Modelling and Measurement of High-frequency Conducted EMI in DC-DC Converters

I. Grobler[1] and M. N. Gitau[2]
Department of Electrical, Electronics and Computer Engineering,
University of Pretoria, Pretoria 0001, South Africa
igrobler@csir.co.za[1], njoroge.gitau@up.ac.za[2]

***Abstract*—** Conducted EMC noise qualification tests are normally carried out after a prototype has been designed, built and tested and the process is repeated in the event of non-compliance. The ability to determine compliance with EMI standards at the design stage is therefore desirable. This paper will present conducted EMC noise modelling and measurement techniques, yielding simulated and measurement noise results accurate enough to serve as a prequalification test at the design and prototyping stages respectively. Accurate models of the power feed-line connecting the LISN to the DUT (converter), including the load are developed. Predictive conducted EMC modelling is accomplished using detailed active level 3 SPICE-based models, creating a real-time circuit model consisting of a complete converter in its operational state, without the need to separate into equivalent models. Effects of the power feed-line length on EMI noise measurements are investigated as currently available literature has not dealt adequately with this issue. To detect possible radiating frequencies that might emerge with the conducted noise and are detectable in the conducted emission test, results have to be accurate not just in the prescribed frequency band, but all the way up to 100 MHz. The modelling and measurements are performed using software and instruments available in a development laboratory.

Keywords— conducted EMC, common-mode, differential-mode, SPICE models, lumped-element, wideband digital measurement, digital noise separation, SiC MOSFET

I. INTRODUCTION

Managing Electro-Magnetic Interferences (EMI) in a power converter should be made an integral part of the design process in order to optimise the overall system design. This improves the design efficiency and shortens the crucial time to market period [1]- [4]. It is also beneficial to be able to model the electromagnetic compatibility (EMC) issues concurrently with the power processor hardware and the thermal management design phase. There is a need therefore, for an affordable, accurate, practical and intuitive EMI modelling and prediction technique suitable for use as an easy design tool [3]. The results obtained using the model should be accurate enough compared to the actual accredited facility measurements [5], building confidence that the converter designed will pass the qualification tests [2], [4].

Most of the readily available EMI models are only concerned with the lower end of the frequency range, up to 10 MHz, as prescribed by MIL-STD-461F or 30 MHz as in the case of CISPR 22 specifications. Extending conducted emission tests into the Very High Frequency (VHF) band, up to at least 100 MHz utilising a high frequency Line Impedance Stabilisation Network (LISN) [6], should help reveal possible radiating effects generated by the converter using the conducted emission test. It is a far easier test to perform in the laboratory than radiated testing. In most cases, and from past experience, radiating problems in power converters occur mostly below 100 MHz, and to a lesser extent, up to 200 MHz. At first, a 1.2 m power feed-line will be analysed and tested, as this is, in our case, the specified product power-cord length for shipping the converter. The effects of using an even shorter feed-line on conducted noise measurements will then be carried out.

Design techniques are reported in [2] using fairly accurate Whole-Link circuit models that are tested up to 30 MHz, but the results are not calibrated. Furthermore, power feed-line and load are not considered. Another circuit model reported in [3] uses ORCAD circuit analysis, showing 1-port results ignoring the ground return as well as the power feed-line effect. In [5] a good predictive conducted EMC modelling method is presented, using an expensive software tool SABER, not readily available in a development laboratory.

Furthermore, the common-mode (CM) and differential-mode (DM) noise separation equations are provided but not defined. Additionally, measurements are not calibrated, raising doubts about the accredited nature of the results. The important power feed-line is also not considered in detail. A high-frequency impedance modelling technique is shown in [7] with very good accuracies up to 30 MHz, based on vector modelling by impedance measurements, providing a very good analysis and complex high order models, but omits the qualification/measurement setup. Further, VHF measurement based frequency component modelling is done in [8], but providing s-parameter results and omitting the power feed-line and LISN. A need thus exist to verify the conducted emission results for accuracy to give confidence that converter will be accredited.

Due to advances in computing power, measurement based impedance models [9], [10] and active lumped-element SPICE modelling of the conducted EMI [11] is shown to be accurate and can easily be incorporated into the power converter design phases. Active modelling incorporates the power converter in its natural operating environment where switching phenomena such as the switching slopes, nonlinear behaviour effects and parasitics are modelled. Component models are acquired by measurement with an impedance analyser up to 13 MHz, and up to 300 MHz with a network analyser. Information is also obtained from datasheets or existing SPICE library models to create reasonably well detailed models. Level 3 SPICE models are imported from the available SPICE libraries from Spectrum Software, to model the active components, or if not listed in the library, aligned with the device datasheet. Circuit simulations are performed with Spectrum Software SPICE circuit simulator and MATLAB utilised for calculations and generating some of the characteristics.

The paper is organised as follows: Section II discusses the theoretical analysis pertaining to time-domain measurements as well as the noise separation expressions. Section III develops high frequency models of the main contributors of conducted emission noise. Validating the models by measurement is presented in section IV and section V ends with the conclusion.

II. THEORETICAL ANALYSIS

A. *EMC Measurements in the Time-domain*

Traditionally, superheterodyne EMC receivers are used to record the EMI spectrum. According to the EMC standards, the measurements are performed by sequentially running through the frequency band, dwelling for several seconds at each frequency bin to be measured. Due to the dwell-time in traditional spectrum analyser measurements, the time-domain measurement system on the other hand yields a reduction in the measurement time [12]. The function of the dwell-time is to measure unwanted noise occurring at irregular intervals. Dwell-time can be simulated by recording multiple digital traces or even setting up an oscilloscope trigger to investigate irregular behaviour. The time-domain EMI measurement technique is based on a broadband analogue-to-digital conversion, in this case accomplished using a digital oscilloscope [13]. This recorded time-based data is further processed by signal processing routines, including the Fast Fourier Transform (FFT), to provide frequency domain results.

B. *Separating Differential and Common-mode Noise*

The two conducted noise emission modes that exist in DC-DC power converters are: the DM and the CM of conduction as defined in Fig. 1 (a) and (b) respectively. A high frequency current probe configured as shown in Figs. 1 (a) and (b) is used to verify the calculated noise signals from the simultaneously digitised measurement of the LISN voltages defined as V_X and V_Y. In Fig. 1 (a), the current probe coil is wired to measure $2I_{DM}$ and in Fig. 1 (b) to measure I_{CM}. The expressions needed to separate differential and common-mode voltages will be derived from first principles to address discrepancies relating to the equations found in the literature. With reference to Fig. 1 (a), an expression for differential-mode current in terms of V_X and V_Y is obtained as:

$$I_{DM} = \frac{I_X - I_Y}{2} = \frac{V_X/50 - V_Y/50}{2} \tag{1}$$

An expression for the differential-mode voltage is obtained in terms of V_X and V_Y as:

$$V_{DM} = V_X - V_Y \tag{2}$$

An expression for converting the differential-mode current to voltage is obtained as:

$$I_{DM} = \frac{V_{DM}}{100} \tag{3}$$

Following a similar approach, the expressions for LISN common-mode current and voltage in Fig. 1 (b) are then obtained as:

$$I_{CM} = I_X + I_Y = V_X/50 + V_Y/50 \tag{4}$$

$$V_{CM} = \frac{V_X + V_Y}{2} \tag{5}$$

The conversion of common-mode voltage to current is achieved using the expression:

$$I_{CM} = \frac{V_{CM}}{25} \tag{6}$$

Equations (2) and (5) are used to separate noise voltage digitally from the LISN measurement ports and is verified with an EMC current probe and is in agreement with those expressions given in [14] - [16]. However, expressions given in other available literature such as [17]-[20] were found to be different, defining the DM noise as half the difference between the phase voltages (i.e. $2.V_{DM} = V_X - V_Y$), causing a 6 dB discrepancy in the noise level. The definition used for noise separation is rarely defined in literature [21], creating a source of confusion.

The step-down converter circuit diagram and LISN schematic is provided in Fig. 1 (c), showing the heatsink connected to the ground plane. A block diagram of the EMC model is given in Fig. 1 (d), which includes the external power source, the LISN circuit, the power feed-line, and the converter elements with its load, above a solid ground plane. Section III will model the parasitic elements.

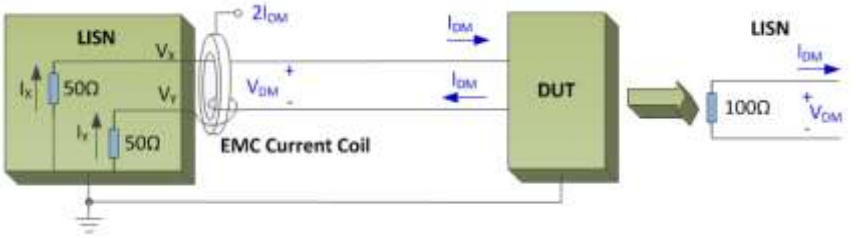

(a)

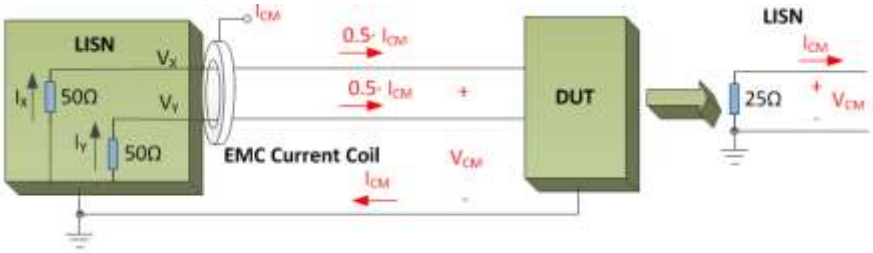

(b)

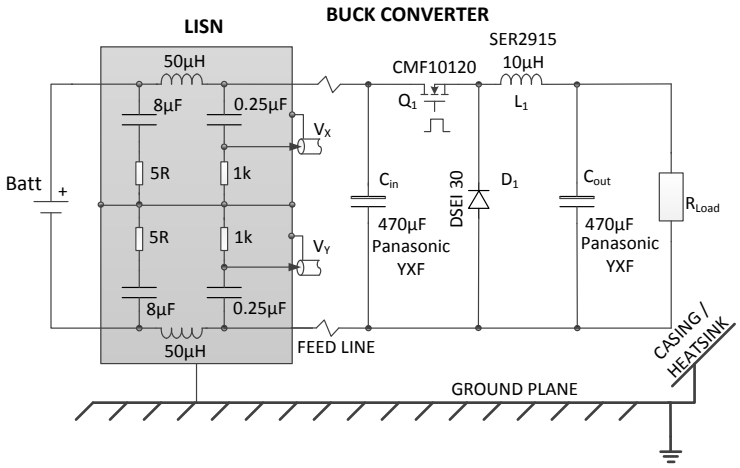

(c)

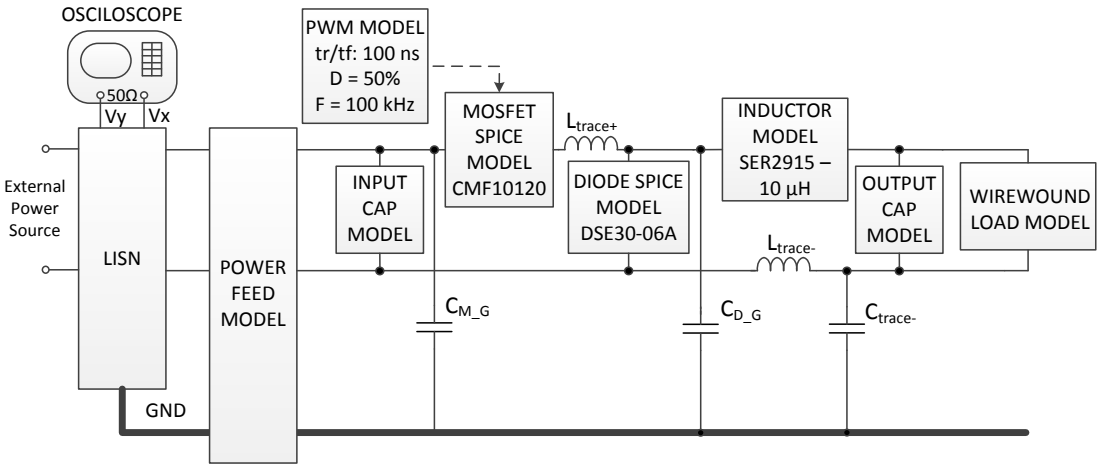

(d)

Fig. 1: The double LISN showing current probe: (a) differential-mode, and (b) common-mode, step-down DC-DC converter LISN and test circuit schematic (c) and EMC test bench block diagram (d).

III. HIGH-FREQUENCY CONVERTER NOISE MODELLING

Simplified circuit models found in the literature [18], [20] are generally accurate only in the lower frequency band of the conducted noise. Therefore, when operating at very high switching frequencies, a new modelling approach is needed to provide more accurate results. A test circuit comprising of a 120 W step-down DC-DC converter with a heatsink, power feed-line and a LISN as shown in Fig. 1 (c) is constructed and used to develop and validate a more accurate modelling procedure for accreditation, with the model block diagram presented in Fig. 1 (d). A lead-acid gel battery suspended on a wooden block, so as not to influence the measurement, provides the auxiliary power for the circuit, which includes the MOSFET driver and PWM controller.

A. Characterising Component Parasitics

All power components and high current tracks that include the LISN to Device Under Test (DUT) power feed-line, are characterised with an impedance analyser HP8656A capable of measuring up to 13 MHz. The higher frequencies on the other hand are characterised with a network analyser HP8753 set at $Z_0 = 50\ \Omega$, characterising components up to 100 MHz and beyond. Scattering parameters, S_{11}, are measured and converted to impedance using the well-known equation [19].

$$Z_{IN} = Z_0 \cdot \frac{1 + S_{11}}{1 - S_{11}} \tag{7}$$

The step-down DC-DC converter passive power components need to be verified for high frequency resonant effects, normally appearing in larger component structures. In this case, no high frequency resonant effects are seen up to 100 MHz, and the classic capacitor and inductor models can be implemented. This order of analysis for this size of components is found to be sufficient to model accurately the conducted emission levels up to 100 MHz. Expression for the impedance of 3-element capacitor model is given in (8).

$$|Z_C| = \sqrt{R_{ESR}{}^2 + \left(\omega \cdot L_{ESL} - 1/\omega \cdot C_0\right)^2}, \tag{8}$$

where C_0 is the capacitance, R_{ESR} the effective series resistance and L_{ESL} the effective series inductance. Fig. 2 (a) presents the impedance characteristics of a 470 µF capacitor high-frequency model, compared with the measured values. The model compares well with measurements all the way up to 300 MHz.

The impedance of the widely used 3-element high frequency inductor can now be calculated, where L_S is the inductor value, C_P the inter-winding parallel capacitance and R_S the winding series resistance. The parallel and series impedances combination are given as:

$$Z_{L1} = \frac{Z_{CP} \cdot \left(Z_{RS} + Z_{LS}\right)}{Z_{CP} + Z_{RS} + Z_{LS}} \tag{9}$$

Which yields:

$$Z_{L1} = \frac{1/j\omega C_P \cdot \left(R_S + j\omega L_S\right)}{R_S + 1/j\omega C_P + j\omega L_S} \tag{10}$$

The magnitude of impedance Z_{L1} can be written as:

$$|Z_{L1}| = \sqrt{\frac{\left(L_S/C_P\right)^2 + \left(R_S/\omega \cdot C_P\right)^2}{\left(R_S\right)^2 + \left(\omega \cdot L_S - 1/\omega \cdot C_P\right)^2}} \tag{11}$$

Expression (11) is plotted in Fig. 2 (b) as Model 1, showing a large infinite peak at resonant frequency that needs to be damped to be comparable to the measured impedance. A 4-element model that adds a damping resistor R_P in parallel compares better with the measured inductor impedance up to 100 MHz. Similarly as the 3-element inductor model, the 4-element model impedance equation can be derived, and is given in (12).

$$Z_{L2} = \sqrt{\frac{\left(R_P \cdot L_S / C_P\right)^2 + \left(R_S \cdot R_P / \omega \cdot C_P\right)^2}{\left(L_S / C_P + R_S \cdot R_P\right)^2 + \left(\omega \cdot L_S \cdot R_P - \left(R_P + R_S\right) / \omega \cdot C_P\right)^2}} \tag{12}$$

For larger sized inductors, a more complex equivalent circuit is needed, increasing to 5- and 7-element circuits when resonating peaks start to occur within the 100 MHz measurement band, as is the case with the load resistor, analysed in section III C.

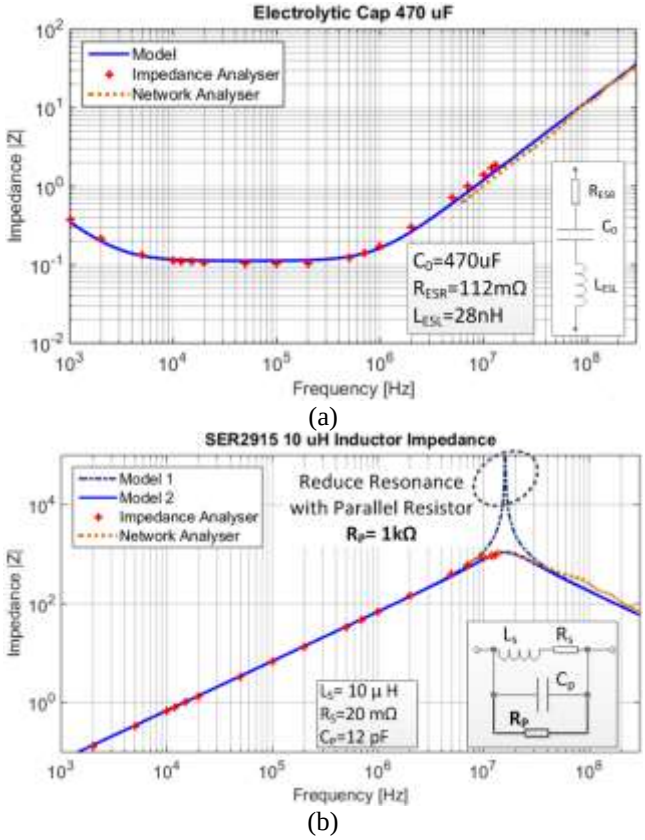

Fig. 2: Classic High-frequency impedance: (a) capacitor, and (b) inductor.

The choice of the active components will have an effect on the converter conducted EMC noise level [11], [22]. The relevant level 3 SPICE models for a vast number of active components are available in Spectrum Software SPICE library. It provides a full explanation of each of the many MOSFET parameters and diode parameters as well as providing a file link to the component data sheet for reference purposes. Devices not listed in the library can be created by using, for example, a similar device and changing the level 3 SPICE

parameters accordingly. Extracting SPICE parameters can also be performed if device datasheets are not complete [23]. Devices parasitic effects, such as leg inductances and component trace capacitances need to be added to the schematic of the SPICE circuit models [10].

B. *Power Feed Line Modelling*

The 2 m power feed-line from the LISN to the DUT prescribed by MIL-STD-461F is not suitable for VHF measurements and need to be shortened. Two lengths will be modelled and measured, one of 1.2 m and a shorter length of 0.30 m. The 1.2 m length is investigated as the end products will normally be shipped with this length of power cable. Due to the possible radiation loss over the 1.2 m model, a 0.3 m cable will also be modelled and compared, as borrowed from the CISPR 15 conducted emission standard dealing with VHF-band conducted emission measurements [24].

The power feed-line from the LISN to the DUT is modelled using a passive distributed network technique. The model is then expanded to incorporate the VHF frequency effects through measurement and iterative impedance fitting. Fig. 3 (a) presents the power feed-line constructed between the LISN and DUT. It is set at a width, *d*, of 20 mm and a length, *l*, of 1.2 m (or 0.3m), and secured onto wooden blocks at a height above ground sheet of 50 mm, according to the standards. This ensures consistent repetitive measurements, as this power feed-line physical routing has a noticeable effect on EMI at high frequencies [25].

Due to the high-frequency transmitted on the power feed-line, the skin effect, δ, will influence the series resistance, and is given by (13), where ω is the radial frequency, σ_c, the conductivity of copper and, μ_c, the permeability of copper.

$$\delta = \sqrt{\frac{2}{\omega \cdot \sigma_C \cdot \mu_C}} \tag{13}$$

The resistance R_f of the power feed-line can now be calculated using (14), where, *a*, is the power feed-line wire radius. Similarly, L_f, C_f, G_f and Z_{in} are given in (15) to (18) [19].

$$R_f = \frac{2}{\sigma_C \cdot 2 \cdot \pi \cdot a \cdot \delta}, \qquad for \qquad a << \delta \tag{14}$$

$$L_f = \frac{\mu_C}{\pi} \operatorname{a\cosh}\left(\frac{d}{2a}\right) \tag{15}$$

$$C_f = \frac{\pi \varepsilon_0}{\operatorname{a\cosh}\left(\frac{d}{2a}\right)} \tag{16}$$

$$G_f = \frac{\pi \cdot \sigma_{air}}{\operatorname{a\cosh}\left(\frac{d}{2a}\right)} \tag{17}$$

The impedance is now given as:

$$|Z_{in}| = \left| \sqrt{\frac{R_f + j\omega L_f}{G + j\omega C_f}} \right| \tag{18}$$

Equations (14) to (18) provide the component values given in Fig. 3 (b). The value R_f is calculated at 1 MHz, and found to be sufficient. These values are then distributed into the 4-cell model in Fig. 3 (b) [26], adding minor adjustments such as the 25 kΩ damping resistor, the 0.1 pF line capacitance and copper ground sheet parameters extracted from the measured impedance plot in Fig 3 (c), incorporating the in-band resonance. The verified impedance plot in Fig. 3 (c) shows the lower frequency measurement obtained with an impedance analyser. The high-frequency effects up to at least 300 MHz, are obtained using a network analyser. These plots are then compared to the ideal model (in Fig. 3 (a)) and the SPICE model in Fig. 3 (b). The effect of shortening this line will also be investigated due to possible in-band radiating effects. Recalculating all the line model parameters for a 30 cm power feed-line provides the simpler model presented in Fig. 3 (d). Fig. 3 (e) depicts the impedance plot for the 30 cm power feed-line. It presents characteristics for the ideal model, the 4-cell SPICE model and the experimental results. The first resonant point on this shorter line lies outside the 100 MHz measurement band.

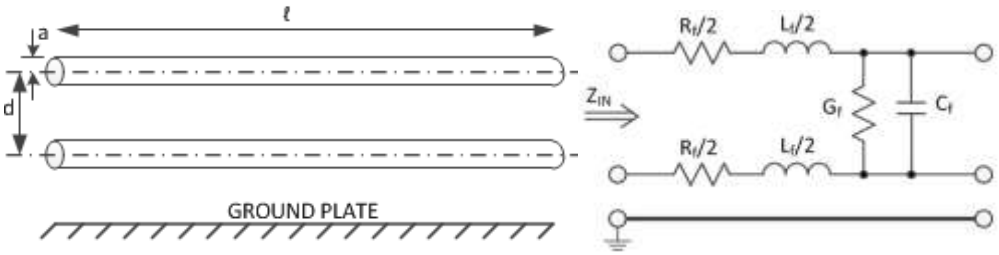
ℓ
a
d
GROUND PLATE
$R_f/2$
$L_f/2$
Z_{IN}
G_f
C_f
$R_f/2$
$L_f/2$

(a)

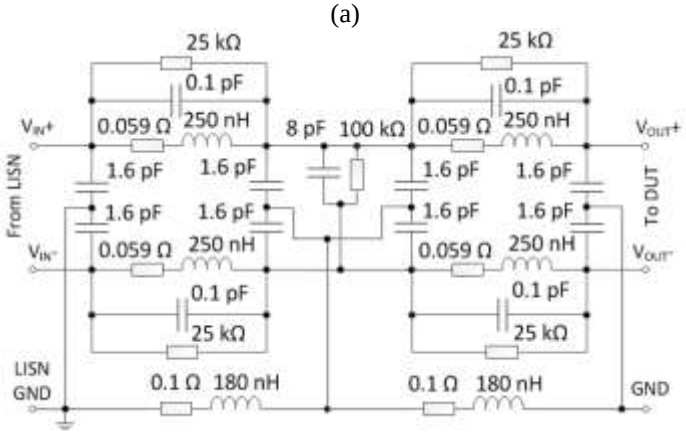
25 kΩ
0.1 pF
V_{IN}+
0.059 Ω
250 nH
8 pF
100 kΩ
0.059 Ω
250 nH
V_{OUT}+
From LISN
1.6 pF
1.6 pF
1.6 pF
1.6 pF
1.6 pF
1.6 pF
1.6 pF
1.6 pF
To DUT
V_{IN}-
0.059 Ω
250 nH
0.059 Ω
250 nH
V_{OUT}-
0.1 pF
25 kΩ
0.1 pF
25 kΩ
LISN
GND
0.1 Ω
180 nH
0.1 Ω
180 nH
GND

(b)

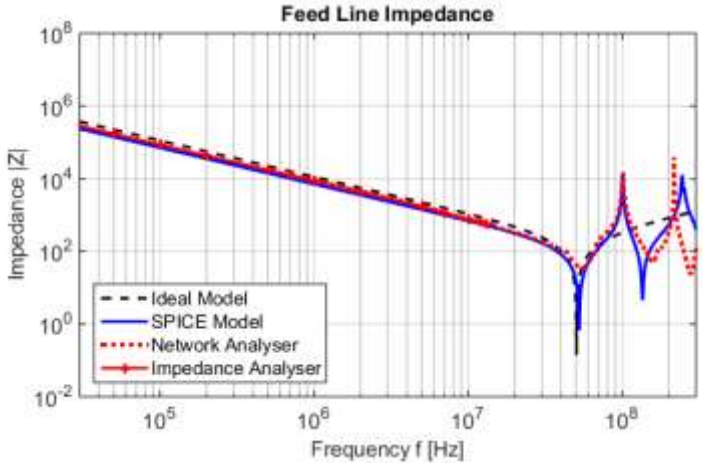
Feed Line Impedance
Impedance |Z|
Frequency f [Hz]
Ideal Model
SPICE Model
Network Analyser
Impedance Analyser

(c)

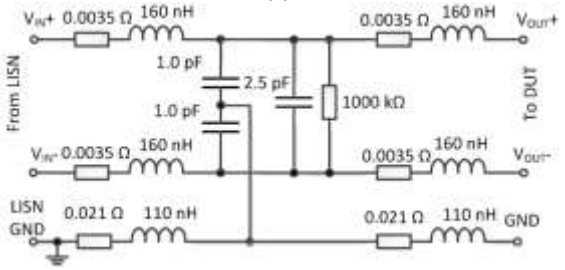
V_{IN}+
0.0035 Ω
160 nH
0.0035 Ω
160 nH
V_{OUT}+
From LISN
1.0 pF
2.5 pF
1000 kΩ
1.0 pF
To DUT
V_{IN}-
0.0035 Ω
160 nH
0.0035 Ω
160 nH
V_{OUT}-
LISN
GND
0.021 Ω
110 nH
0.021 Ω
110 nH
GND

(d)

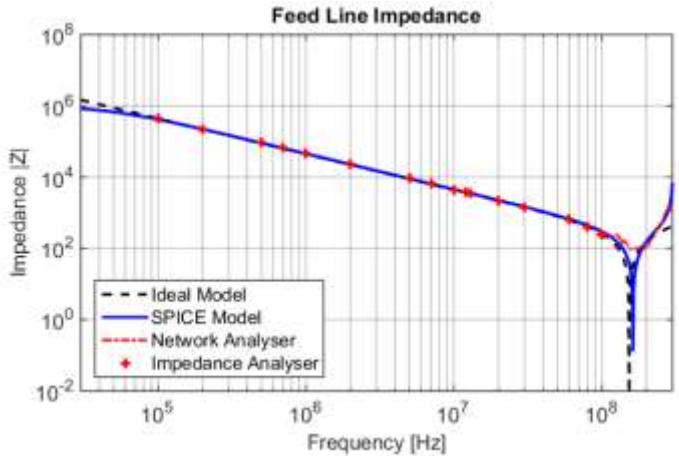

(e)

Fig. 3: (a) Power feed-line and simplified model, (b) 1.2 m power cable lumped-element model (c) impedance characteristics, (d) 30 cm power cable lumped-element model and (e) its impedance characteristics.

C. Load Characterisation

The 200 W 16-Ω wire-wound load are characterised as it plays a role in the power converter and subsequent noise characteristics. The equivalent SPICE-based model need to include the parasitics, as it shows a correlation between the geometry and the parasitic circuit elements [8]. The measured impedance showing multiple resonant points is turned into a higher order equivalent circuit model by using a vector fitting technique [7] . The measurement based model of the load is shown in Figs. 4 (a) and (b) and the verification plots in Fig. 4 (c). The 4-element model shows the load resistance, a series inductance of 27 µH, a parallel capacitance of 8 pF as well as a parallel damping resistor of 25 kΩ. Above 10 MHz multiple resonant points occur due to the larger physical structure of the load. Accurate modelling of the load needs at least a 9-element model, disseminated from the 4-element model, as shown in Fig. 4 (b) and consequent impedance characteristics in Fig. 4(c). The load is suspended on wooden blocks to minimise the capacitance to the copper ground-sheet.

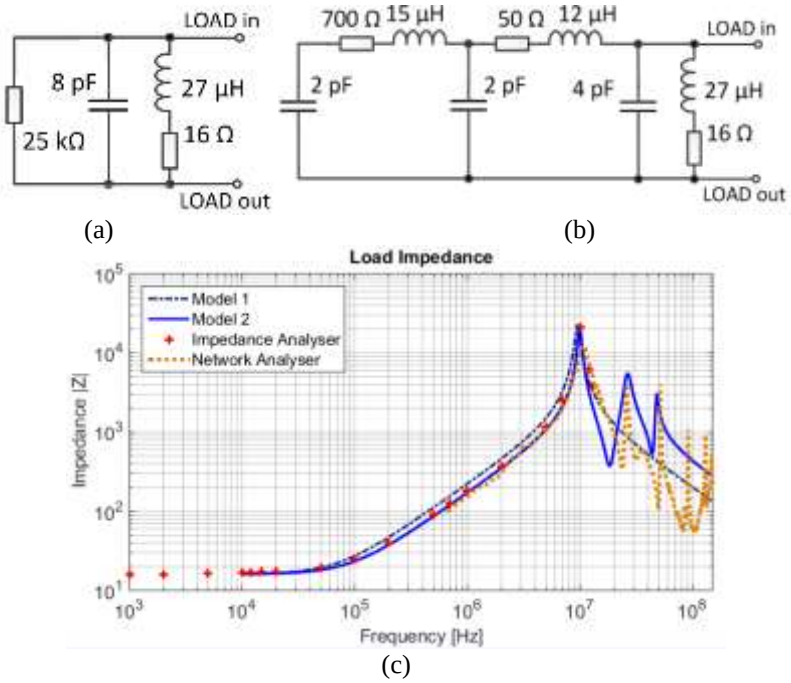

Fig. 4: Wire-wound load equivalent circuit: (a) 4-element Model 1, (b) 9-element Model and (c) impedance verification plots.

D. Heatsink Characterisation

The heatsink capacitance-to-ground plays a crucial role in both the generation and propagation of the common-mode noise, and can be estimated with the parallel-plate capacitance equation as given in (19).

$$C_H = \frac{\varepsilon_0 \varepsilon_r A}{s}, \tag{19}$$

where ε_0 is the permittivity of air and ε_r is the permittivity of the heatsink insulator, taken as 2.9 for silpad, A is the surface area of the MOSFET tab and s the insulator thickness. Fig. 5 (a) shows the physical layout of the MOSFET and the diode on the heatsink, defining the tab capacitance to the heatsink as C_{HM} and C_{HD} for the MOSFET and diode respectively. Fig. 5 (b) shows the tab of the diode, dimensions 16.8 mm by 14.2 mm, minus the mounting hole with diameter 6.5 mm. The tab is 2 mm thick. The MOSFET tab is similar and thus not presented. With an insulator thickness of 0.15 mm, the tab to heatsink capacitance for both the MOSFET and the diode works out as 40 pF each.

Fig. 5 (c) shows the capacitance values of the diode- as well as the MOSFET tab to the heatsink. In both cases the screw fastener torque was set to 0.7 N-m. No resonant effects are observed within the measured frequency band.

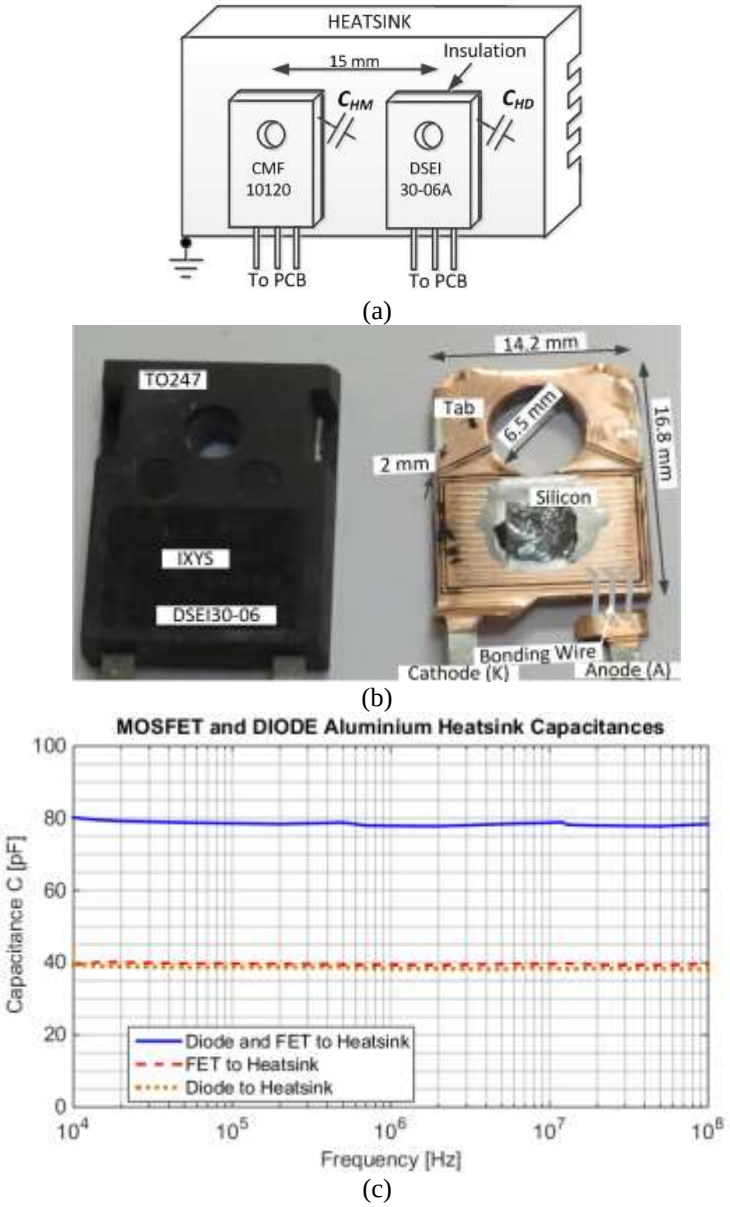

Fig. 5: (a) Physical device layout on heatsink, (b) device tab exposed and (c) device to heatsink capacitance verified.

E. Conducted Emission Model

The individual models of the converter's main sub-components and peripherals such as the power feed-line and the load created in the preceeding sections are combined in a parasitic element SPICE circuit producing a complete model of the converter in its EMC test environment.

Fig. 6 (a) shows the HF step-down converter SPICE model. The load, power feed-line and the LISN is not shown in this diagram, but is loaded in the SPICE model. The gate switching-voltage is programmed for 80 ns rise-and fall times, pulse width 4.5 µs and period 7.6 µs, corresponding to the prototype circuit parameters. The model circuit can be simplified by utilising the internal SPICE parasitic models from Spectrum Soft. The SiC MOSFET model has to be created and the SPICE level 3 parameters are given in Fig. 6 (b). The descriptions of the model parameters are provided by hovering over the value in Spectrum Software SPICE window. The diode, DSIE30-06A, SPICE level 2 model parameters from the Spectrum Software circuit model are provided in Fig. 6 (c). The capacitor and inductor parasitic components are added externally in this case, but the SPICE models for these components incorporating the parasitic effects may also be used, as shown in Fig. 6 (d) for the input capacitor, but only 3-element models are available, and not useful when a 4-element parasitic model is needed, such as in the case of the inductor.

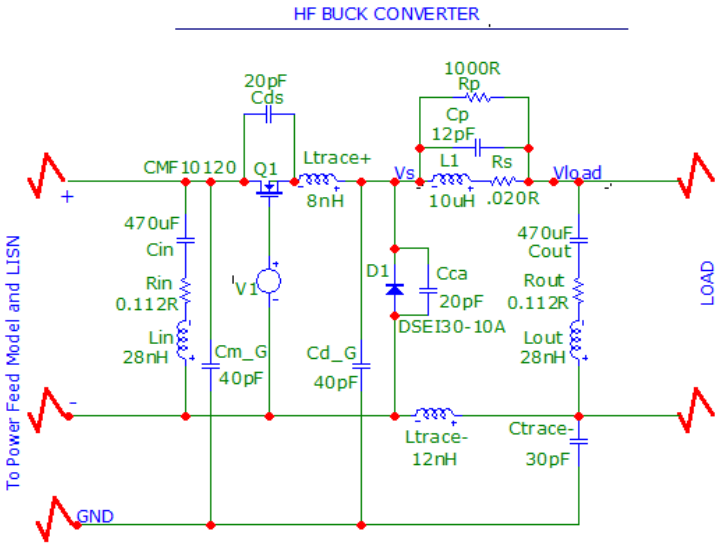

(a)

Source: Local page 'Models'

LEVEL	3	AF	1	CBD	1n
CBS	0	CGBO	0	CGDO	500p
CGSO	0.59n	CJ	0	CJSW	0
DELTA	0	ETA	0	FC	500m
GAMMA	0	GDSNOI	0	IS	10f
JS	10n	JSW	0	KAPPA	undefined
KF	0	KP	20u	L	2u
LAMBDA	394f	LD	0	MJ	500m
MJSW	330m	N	1	NEFF	1
NFS	0	NLEV	0	NSS	undefined
NSUB	0	PB	800m	PBSW	800m
PHI	600m	RB	0	RD	160m
RDS	800k	RG	8	RS	300m
RSH	0	T_ABS	undefined	T_MEASURED	undefined
T_REL_GLOBAL	undefined	T_REL_LOCAL	undefined	THETA	0
TOX	0	TPG	1	TT	0
UCRIT	10K	UEXP	0	UO	600
UTRA	0	VMAX	0	VTO	4
W	850m	WD	0	XJ	0
XQC	1				

(b)

Source: Local page 'Models'

LEVEL	2	AF	1	BV	70
CJO	13p	EG	1.11	FC	500m
IBV	1p	IBVL	0	IKF	0
IS	10e-15	ISR	0	KF	0
M	500m	N	2	NBV	1
NBVL	1	NR	2	RL	5G
RS	5	T_ABS	undefined	T_MEASURED	undefined
T_REL_GLOBAL	undefined	T_REL_LOCAL	undefined	TBV1	0
TBV2	0	TIKF	0	TRS1	0
TRS2	0	TT	1n	VJ	900m
XTI	1				

(c)

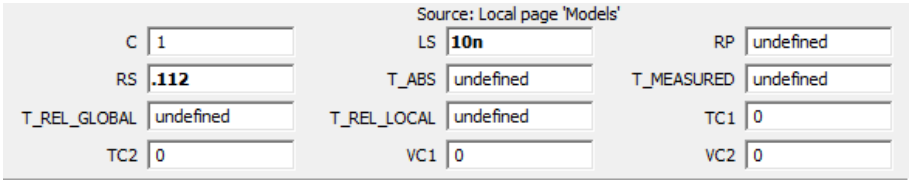

(d)

Fig. 6: (a) Buck converter active SPICE model, (b) MOSFET SPICE parameters (c) diode SPICE parameters and (d) input capacitor model.

IV. MEASUREMENTS

A series of measurements are performed to validate the theoretical analysis. The complete conducted emission SPICE model is created and simulations carried out followed by verifications using practical measurements. A small high-frequency 50 μH/50 Ω ring-core LISN calibrated to 100 MHz [6] and earthed copper sheet bench setup, according to MIL-STD-461F specifications [27], is manufactured and implemented. These are used to verify all simulated data. A Tektronix MDO4034B oscilloscope consisting of four 11-bit analogue channels at 2.5 GS/s each and one frequency spectrum channel is used to record the data. MATLAB is used as a signal-processing tool for analysing the recorded data and calculating the spectral slopes [12], [13], [28]-[30]. The common-mode and differential-mode currents are verified with a high frequency current probe, an ETS Lindgren model 94111-1L. The wideband FFT technique is important to verify and will be compared to a calibrated accredited measurement.

A. SPICE Model Verification

The converter model is actively switched and operates as intended. The LISN ports V_X and V_Y are simultaneously recorded during simulations and the recordings are then transformed into peak spectral slopes with signal processing routines [13], and comparisons carried out. Apart from the V_X and V_Y signals that need to comply with the EMC limits, CM and DM signals are also extracted. The bench setup and the short 30 cm power feed-line are shown in Fig. 7 (a). A weight on the LISN creates an improved ground plate contact. The auxiliary battery and load are suspended on wooden blocks as to minimise their effect on the common-mode return path. Before commencing with measurements, it is advisable to do a noise floor scan,

with all power to the DUT disconnected. The noise floor of the measurement bench is provided in Fig. 7 (b), well below the MIL-STD-461F slope. Fig. 7 (c) shows the LISN V_X port time signal comparison, a slight switching frequency offset is visible, due to component tolerances in the physical prototype circuit. An enlarged portion of the switching transient is shown in Fig. 7 (d), apart from the timing offset, a good correllation is seen.

The comparison between the SPICE V_X port modelled noise results and the actual measurements is shown in Fig. 7 (e). The characteristics extend to just over 100 MHz to show the accuracy achieved with the SPICE model, predicting the frequency spike at 110 MHz, where this is actually the upper limit of the model and measurement capability. The overall plot shows very good agreement with the actual measurements. The discrepancy in amplitude over the middle frequencies, between 10 and 11 MHz, seems to be due to the SPICE MOSFET model that differs slightly from the actual device. This is similar to the slightly higher predicted amplitude between 40 and 70 MHz. Replacing the diode model with a slower device was shown to reduce the predicted spectral amplitude in this band. Similarly, reducing the SPICE model trapezoidal fall-time yields similar results.

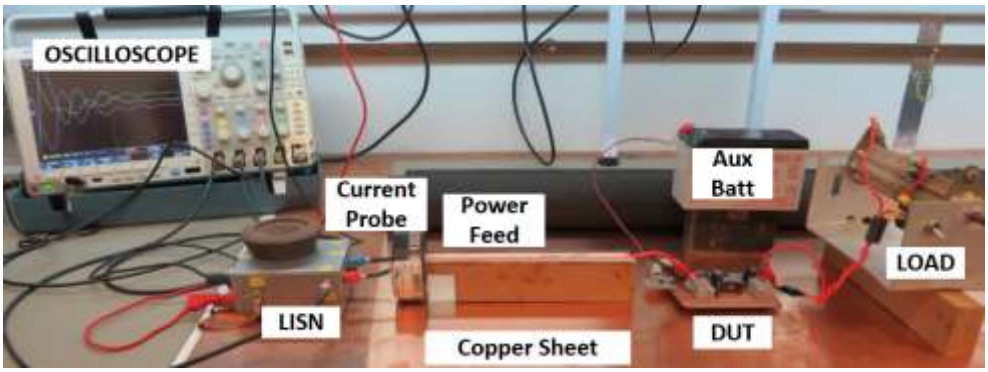

(a)

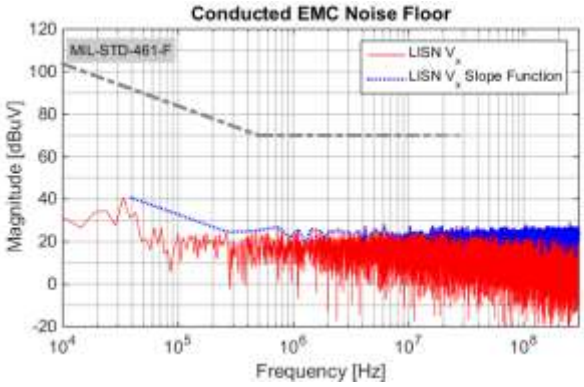

(b)

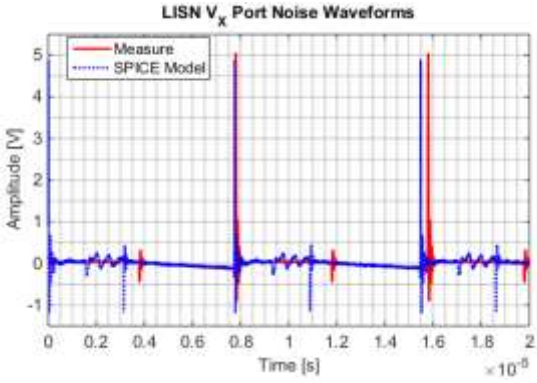

(c)

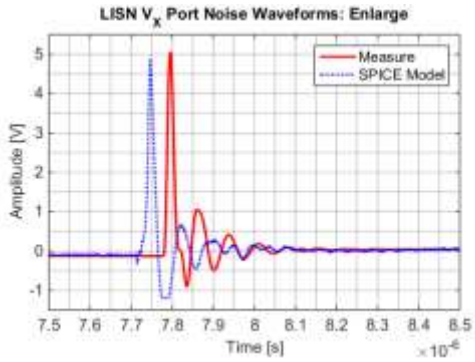

(d)

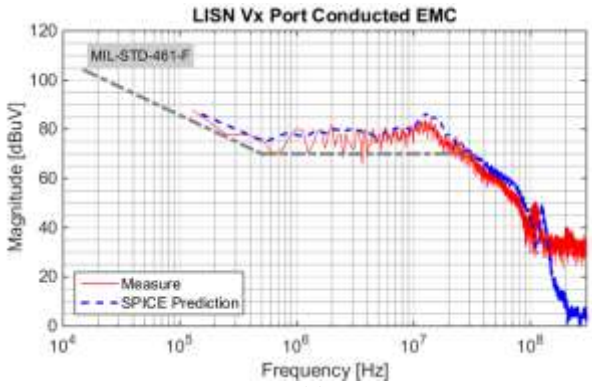

(e)

Fig. 7: (a) Test bench, (b) noise floor with slope function, (c) LISN V_X port model and measurement comparison time base plot, (d) enlarged transient and (e) port V_X spectral slope.

B. Wideband FFT Laboratory Verification

The laboratory time-domain measurement and consequent wideband FFT signal processing spectral slope need to be verified for accuracy. The test circuit was taken to a calibrated EMC facility, known as Houwteq in the Cape Province of South Africa. The MIL-STD-461F setup procedure is subsequently followed, but with a 1.2 m power-feed line. The conducted EMC measurements are recorded with a standard EMC spectrum analyser set to measure dBµV, but deviated from the usual 10 MHz upper band to a frequency of 100 MHz. The results from the LISNs V_X ports of the two different measurement techniques are compared to each other. The solid line in Fig. 8 (a) shows the spectral slope function from the wideband laboratory measurement and the dotted line the spectral slope from the accredited measurement performed with an EMC spectrum analyser. Above 50 MHz, the accredited measurement shows a lower value, due to the high-power dual LISN at the accredited laboratory that is specified only up to 50 MHz. The laboratory LISN on the other hand, is manufactured for up to 100 MHz [6]. A very good agreement exists between the two measurement techniques confirming that the proposed conducted EMC pre-qualification technique is capable of yielding acceptable results.

C. Common-mode and Differential-mode Verification

The voltages V_X and V_Y from the laboratory LISN are recorded on channels 1 and 2 simultaneously with an MDO4043B oscilloscope. The third channel records the current probe information. The signals are split into common- and differential-mode using (2) and (5) and compared to the current probe EMC current coil readings for the configuration shown in Fig. 1 (a) and (b). The comparison between the two measurements is shown in Figs. 8 (b) and (c), plotted in dBµA. The current probe measurements and the calculated LISN data, common-mode as well as differential-mode, are comparable up to 100 MHz, thus validating the accuracy of the derivations (2) and (5). It is thus possible to calculate the differential- and common-mode signals from the LISN ports without the use of a current probe provided they are recorded simultaneously. This is an

important contribution as it provides engineers with alternative methods to obtain common-mode and differential-mode noise signals.

Fig. 8 (d) shows an interesting result for common-mode conducted emission for two conditions, the 1.2 m power feed-line (solid trace) compared to the shorter 30 cm power feed-line. Around 50- 60 MHz, higher common-mode conducted emission amplitudes are measured for the shorter power feed-line. Fig. 8 (e) shows the power feed-line over ground plane scattering parameter reflection coefficient S_{11}, and confirms the 1.2 m feed-line radiating effects occurring between 50- 60 MHz, due to it being a quarter wavelength long at that frequency. At this frequency, the standing wave currents are lower as measured at the LISN ports, attenuating the measured common-mode conducted signal. Fig. 8 (f) confirms the radiating effects of the 1.2 m feed-line, measured at a distance of 3 m from the bench setup with an un-calibrated antenna, recorded with a Rohde&Schwarz FSH3 spectrum analyser. The 0.3 m feed-line shows no measurable radiating phenomena up to 100 MHz.

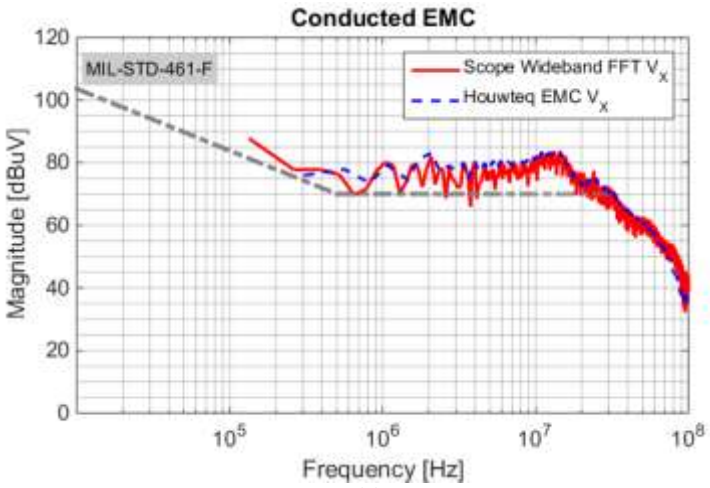

(a)

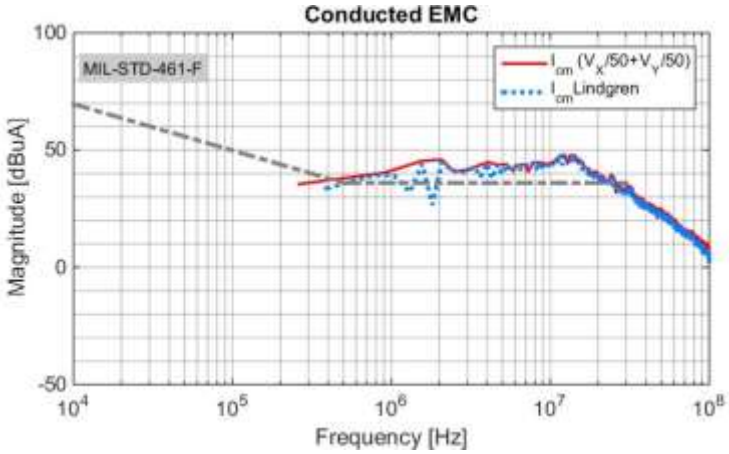
Conducted EMC
MIL-STD-461-F
I_{cm} (V_X/50+V_Y/50)
I_{cm} Lindgren
Magnitude [dBuA]
Frequency [Hz]

(b)

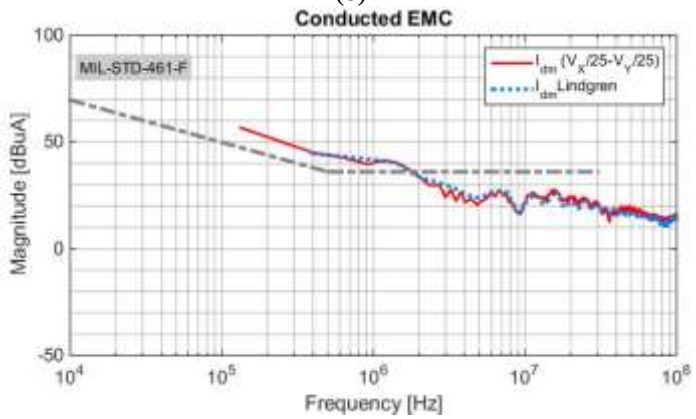
Conducted EMC
MIL-STD-461-F
I_{dm} (V_X/25-V_Y/25)
I_{dm} Lindgren
Magnitude [dBuA]
Frequency [Hz]

(c)

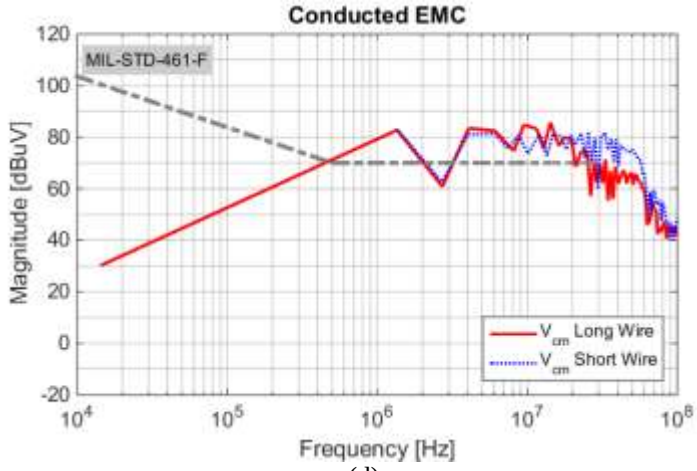
Conducted EMC
MIL-STD-461-F
V_{cm} Long Wire
V_{cm} Short Wire
Magnitude [dBuV]
Frequency [Hz]

(d)

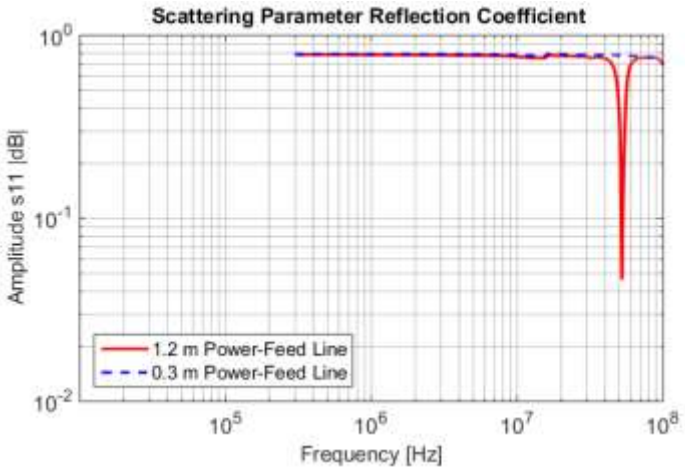

(e)

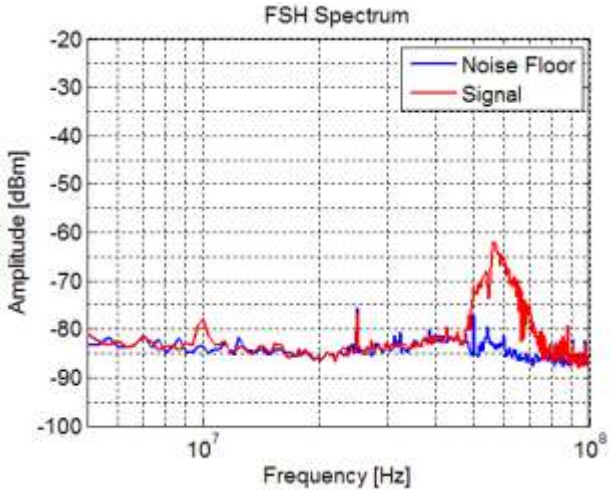

(f)

Fig. 8: Measurement technique comparison: EMC laboratory measurement vs. accredited measurement (a), verification of noise signal separation calculations (b) CM and (c) DM, (d) shorter power feed-line CM effect, (e) power feed-lines scattering parameter S_{11} and (f) un-calibrated radiating effects.

V. CONCLUSION

A laboratory based affordable high-frequency conducted EMC modelling and measurement technique based on the MIL-STD-461F requirement was developed and verified for accuracy. Through the verification procedure, that entailed a comparison with results from an accredited measurement facility, it was demonstrated to be suitable for EMC pre-qualification at the design and prototyping stages. This simplifies determining whether the DUT will pass or fail the conducted EMC verification tests, before constructing a prototype. A wide-band digital measurement technique is compared to the traditional EMC spectrum analyser method, showing the limitation in terms of the achievable noise floor, but still well suited for performing

laboratory measurements with a dynamic range within the conducted EMC limits. The wideband digital measurement process showed that a much faster and accurate analysis method over the standard EMC spectrum analyser technique can be implemented with confidence.

Most of the EMC analysis and optimisation techniques available in literature are only dealing with certain aspects of a converter, showing comparative results of improvement. However, verifying the conducted EMC aspects in a development laboratory environment that is according to the EMC test standards resulting in calibrated levels has not been reported and is of significance. It provides crucial information on whether the converter will pass or fail the conducted emission accreditation test and, furthermore, yields levels of common-mode and differential-mode information to be utilised for optimal filter design, not possible in the standard EMC receiver test setup. The comparison yielded very good accuracies, confirming which of the LISN ports noise mode equations available in the literature are accurate.

Verified and calibrated conducted EMC modelling and measurements were performed beyond the standard 10 MHz or 30 MHz upper frequency limit (up to 100 MHz), providing information on possible radiating effects that might occur. High frequency band measurement based impedance modelling showed that for larger components, such as the power feed-line and the load, VHF resonant effects occur and higher order models are needed. A dynamic SPICE-based circuit incorporating parasitic effects was created representing the modelled power converter in its accredited measurement operating state, without creating separate models for each. The SPICE model conducted emission noise are compared to bench measurements and in turn, compared to a calibrated conducted emission noise level scan at an accredited EMC facility, showing the accuracies achieved from the SPICE model as well as from the bench measurement. Due to the good correlation between the SPICE model and the practical measurements, the model can be utilised to investigate the main contributing factors to conducted EMI. Care should be taken using model parameters directly from the SPICE libraries, as this can cause slight discrepancies. The 1.2 m power feed-line as given, showed resonant effects within the VHF frequency band, and was modelled as such. It was shown that an

improved power feed-line length of 0.3 m is best suited for conducted emission measurements beyond 30 MHz and up to 100 MHz, assisting in higher frequency-span filter design to curb radiating effects that might occur.

The modelling method can be extended to other converter topologies, including multi-phase, multilevel and combined converters. As the simulation results are adequately validated, there is a high degree of confidence that the simulation process as well as a verified measurement setup will lead to an accurate EMC design process. Models can further be optimised taking component proximity effects into account, especially more prominent in larger sized power converters.

REFERENCES

[1] X. J. Lai, X. Huang, E. Pepa, S. Chen and T. W. Nehl, “Inverter EMI modelling and simulation methodologies,” IEEE Transactions on Industrial Electronics, Vol. 53, No. 3, pp. 736-744, June 2006.

[2] Y. Zhou, Y. Zhu, Q. Song, Z. Jin, D. Yang and X. Yu, "Prediction and reduction of electromagnetic conducted emission in active clamp forward converter", IEEE Electromagnetic Compatibility (EMC) Symposium, Long Beach, USA, pp. 729-733, 14-19 Aug. 2011.

[3] K. R. A. Britto, R. Vimala, R. Dhanasekaran and B. Saranya, "Modelling of conducted EMI in flyback switching power converters", IEEE, Electronics and Control Engineering (ICONRAEeCE), Sivakasi, pp. 377- 383, 15-17 Dec. 2011.

[4] T. Williams, "Characterisation of emissions due to power electronics heatsinks," International Symposium on Electromagnetic Compatibility, Brugge, pp. 616-621, 2-6 Sept. 2013.

[5] E. Rondon- Pinilla, F. Morel, C. Vollaire and J. Schanen, "Modelling of a Buck Converter With a SiC JFET to Predict EMC Conducted Emissions," IEEE Transactions on Power Electronics, Vol. 29 , No. 5, pp. 2246 – 2260, May 2014.

[6] I. Grobler, M. N. Gitau, “Low cost power lead extended pre-compliance conducted EMI measurement setup and diagnostics with compact LISN”, IEEE ECCE Asia Down Under, Melbourne, pp. 1144 – 1149, 3-6 June 2013.

[7] K. Jia, G. Bohlin, M. Enohnyaket, R. Thottappillil, "Modelling an AC motor with high accuracy in a wide frequency range", IET Electric Power Applications, Volume 7, Issue 2, pp. 116 – 122, Feb. 2013.

[8] L. Li, B. Xu, N. Bondarenko, G. Li, T. Makharashvili, D. Loken, P. Berger, T. Van Doren, D. Beetner, "A Measurement-Based Model of the Electromagnetic Emissions from a Power Inverter", IEEE Transactions on Power Electronics, no.99, pp. 1-10, 2013.

[9] X. Gong and J. A. Ferreira, "Extracting the parameters of a common-mode EMI equivalent circuit model for a drive inverter", Power Electronics Conference (IPEC), Sapporo, pp. 892-899, 21-24 June 2010.

[10] A. Cataliotti, D. Di Cara, G. Marsala, A. Pecoraro, A. Ragusa, G. Tine` - High-Frequency Experimental Characterization and Modeling of Six Pack IGBTs Power Modules” - IEEE Transaction on Industrial Electronics, Vol. 63, No. 11, Nov. 2016.

[11] J.B.H. Slama and M. Tlig, "Effect of the MOSFET choice on conducted EMI in power converter circuits", IEEE Electrotechnical Conference (MELECON), Mediterranean, Tunisia, pp. 610-613, 25-28 March 2012.

[12] P. Russer, "EMC measurements in the time-domain", IEEE General Assembly and Scientific Symposium, Istanbul, pp. 1-35, 13-20 Aug. 2011.

[13] C. Keller and K. Feser, ‘Fast Emission Measurement in Time-domain’, IEEE Transactions on Electromagnetic Compatibility, Vol. 49, No. 4, pp. 816 – 824, Nov. 2007.

[14] A. Kempski, R. Smolenski, "Decomposition of EMI Noise into Common and Differential-modes in PWM Inverter Drive Systems", Journal Electric Quality and Utilisation, Vol. XII, No. 1, pp. 53-58, 2006.

[15] A.S. de Beer, G. N. Wooding, J.D. van Wyk, "Problematic Aspects when using a LISN for Converter EMI Characterisation", IEEE International Conference on Industrial Technology, Cape Town, pp. 633-637, 25-28 Feb. 2013.

[16] M. C. Caponet, F. Profumo, L. Ferraris, A. Bertoz, D. Marzella, "Common and differential-mode noise separation: comparison of two different approaches", Power Electronics Specialists Conference, Vancouver, Vol. 3, pp. 1383 - 1388, 17-21 June 2001.

[17] P. R. Clayton, "Introduction to Electromagnetic Compatibility", Second Edition, John Wiley and Sons, Inc. Publication, 2006.

[18] R. Vimala, K. Baskaran and K. R. Aravind Britto, “Modeling and Filter Design through Analysis of Conducted EMI in Switching Power Converters”, Journal of Power Electronics, Vol. 12, No. 4, July 2012.

[19] P. L. D. Abrie, “The design of impedance-matching networks for radio-frequency and microwave amplifiers,” Artech House, Inc., 1985, Chapter 1, 7.

[20] M. Jin, M. Weiming, P. Qijun, K. Jun, Z. Lei and Z. Zhihua, "Identification of Essential Coupling Path Models for Conducted EMI Prediction in Switching Power Converters”, IEEE Transaction on Power Electronics, Dubrovnik, Croatia, Vol. 21, pp. 1795-1803, 20-23 June 2006.

[21] K. Kostov, H. Nee and M. Priecinsky, "The Input Impedance of Common Mode and Differential Mode Noise Separators", IEEE Transactions On Industry Applications, Vol. 51, No. 3, pp 2352 - 2360, June 2015.

[22] W. Teulings and B. Vrignon, "Fast conducted EMI prediction models for smart High-Side Switches", 8th Workshop on Electromagnetic Compatibility of Integrated Circuits (EMC Compo), Dubrovnik, pp. 159-164, 6-9 Nov. 2011.

[23] M. D. Hasanuzzaman, S. K. Islam, L. M. Tolbert, B. Ozpineci, "Design, Modeling, Testing, And Spice Parameter Extraction of Di-MOS Transistor in 4h-Silicon Carbide", International Journal of High Speed Electronics and Systems, No 16, pp 733-737, 2006.

[24] CISPR 15:2009, Edition 7.2, “Limits and methods of measurement of radio disrurbance characteristics of electrical lighting and similar equipment”, International Special Committee on Radio Interference.

[25] A. Ales, J. Schanen, D. Moussaoui, and J. Roudet, “Impedances Identification of DC/DC Converters for Network EMC Analysis”, IEEE Transactions on Power Electronics, Vol. 29, No. 12, pp. 6445 - 6457, Dec. 2014.

[26] I. Grobler and M.N. Gitau, “Conducted EMC Modeling for Accreditation in DC-DC Converters,” IEEE Industrial Electronics Society IEEE IECON, Yokohama, Japan, pp. 2329 - 2335, 9-12 Nov. 2015.

[27] MIL-STD-461F, "Requirements for the Control of Electromagnetic Interference Characteristics of Subsystems and Equipment", Dept of Defense Interface Standard, December 2007.

[28] S. Braun, "An Overview of Emission Measurements in Time-domain", IEICE EMC Kyoto, Japan, pp. 681 - 684, 20-24 July 2009.

[29] F. Krug, T. Hermann, and P. Russer, “Signal Processing Strategies with the TDEMI Measurement System,” in 2003 IEEE Instrumentation and Measurement Technology Conference Proceeding, , Vail, USA, pp. 832–837, 20–22 May 2003.

[30] C. Hoffmann and P. Russer, "A low-noise high dynamic-range time-domain EMI measurement system for CISPR Band E", Advances in Radio Science, No. 9, pp. 309–315, Aug. 2011.